ODAR: Aerial Manipulation Platform Enabling Omnidirectional Wrench Generation

Sangyul Park, Jeongseob Lee, Joonmo Ahn, Myungsin Kim, Jongbeom Her, Gi-Hun Yang, and Dongjun Lee

***Abstract*—We propose a novel aerial manipulation platform, an omnidirectional aerial robot, that is capable of omnidirectional wrench generation with opportunistically distributed/aligned Sectional rotors. To circumvent the tight thrust margin and weight budget of currently available rotor and battery technologies, we propose a novel design optimization framework, which maximizes the minimum-guaranteed control force/torque for any attitude while incorporating such important and useful aspects as interrotor aerointerference, anisotropic task requirement, gravity compensation, etc. We also provide a closed-form solution of infinity-norm optimal control allocation to avoid rotor saturation with the tight thrust margin. Further, we elaborate the notion of electronic speed controller induced singularity and devise a novel selective mapping algorithm to substantially subdue its destabilizing effect. Experiments are performed to validate the theory, which demonstrate such capabilities not possible with typical aerial manipulation systems, namely, separate translation and attitude control on SE(3), hybrid pose/wrench control with downward force of 60 N much larger than its own weight (2.6 kg), and peg-in-hole teleoperation with a radial tolerance of 0.5 mm.**

***Index Terms*—Aerial manipulation, design optimization, fully actuated platform, reversible electronic speed controller (ESC), selective mapping.**

I. Introduction

MULTIROTOR unmanned aerial vehicles (UAVs) or simply drones have received booming interests from the research community and the general public alike due to their capacity/promise to extend our sensory and manipulation ability to the three-dimensional (3-D) space without being bound to the ground. This flourishing field of drones is enabled by the recent advancement and maturation of many background technologies, including material/manufacturing (e.g., carbon fiber and magnesium alloy), sensors (e.g., microelectromechanical systems, inertial measurement unit (IMU), sonar, cameras, etc.), actuators (e.g., brushless direct current (BLDC) motors, on-board computing and communication, and algorithms (e.g., sensor fusion, localization, control, image processing, etc.), to name just a few.

The most successful applications of the drones so far are mostly "seeing" applications, including aerial photography, geosurveying, traffic monitoring, etc. However, to truly extend the usefulness of the drones to the 3-D space, it is necessary to endow them with the ability of aerial manipulation, and for that, drone-manipulator systems (i.e., drone with multidegree-of-freedom (DOF) robotic arm) are most intensively investigated [1]–[4]. This drone-manipulator system, yet, suffers from the following two crucial limitations stemming from the underactuation of the drone (i.e., it cannot control its position and orientation at the same time with all axes of rotors parallel): it would not be able to maintain contact or continue manipulation task when there blows a side-way gust, since it cannot hold its orientation in the presence of lateral disturbance, particularly given that the attached robotic arm is typically of only low-DOF due to the payload limitation of the drone; and it cannot exert downward force larger than its own weight and can do so only by turning off its rotors, since, for typical drones, all the rotors are aligned upward and driven by unidirectional electronic speed controllers (ESCs), although this downward force is very important for many practical applications. These limitations, we believe, are because the multirotor drone platforms are designed/optimized for ease of flying, not for manipulation.

To overcome these limitations of the conventional multirotor drones, in this paper, we propose a novel flying platform for aerial manipulation, the omnidirectional aerial robot (ODAR), as shown in Fig. 1. By utilizing opportunistically aligned/distributed bidirectional rotors (with reversible ESC and bidirectional props), this system can attain omnidirectional motion (i.e., arbitrary position/orientation) or produce omnidirectional wrench (i.e., arbitrary force/torque). This full-actuation in SE(3) allows for such practically useful behaviors not possible with other typical aerial operation systems:

1) exerting force/torque in all directions, particularly pushing from the top (e.g., structure maintenance/repair);

Manuscript received July 26, 2017; revised February 15, 2018; accepted May 6, 2018. Date of publication July 2, 2018; date of current version August 14, 2018. Recommended by Technical Editor Y. Shi. This work was supported in part by the Basic Science Research Program of the National Research Foundation of Korea funded by the Ministry of Science, ICT & Future Planning under Grant 2015R1A2A1A15055616, in part by the Industrial Strategic Technology Development Program under Grant 10060070, and in part by the Industrial Convergence Core Technology Development Program of the Ministry of Trade, Industry & Energy of Korea under Grant 10063172. *(Corresponding author: Dongjun Lee.)*

S. Park, J. Lee, J. Ahn, M. Kim, and D. Lee are with the Department of Mechanical and Aerospace Engineering and Institute of Advanced Machines and Design, Seoul National University, Seoul 08826, South Korea (e-mail: sangyul@snu.ac.kr; overjs94@snu.ac.kr; ahnjmo1993@snu.ac.kr; myungsinkim@snu.ac.kr; djlee@snu.ac.kr).

J. Her is with Samsung Electronics, Suwon 16677, South Korea (e-mail: jongbeom.her@samsung.com).

G.-H. Yang is with the Korea Institute of Industrial Technology, Ansan 15588, South Korea (e-mail: yanggh@kitech.re.kr).

Color versions of one or more of the figures in this paper are available online at http://ieeexplore.ieee.org.

Digital Object Identifier 10.1109/TMECH.2018.2848255

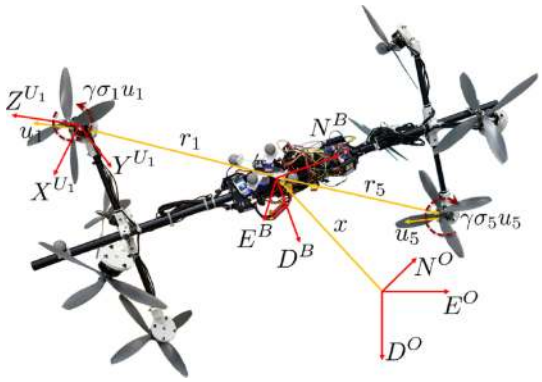

Fig. 1. ODAR system with eight nonaligned bidirectional rotors as obtained from the design optimization (4). Also shown are the inertial, body, and ith rotor coordinate frames $\{O\} := \{N^O, E^O, D^O\}$, $\{B\} := \{N^B, E^B, D^B\}$, and $\{U_i\} := \{X^{U_i}, Y^{U_i}, Z^{U_i}\}$, $i \in \{1, ..., 8\}$; and the orientation, position, and reaction momentum vectors of the ith rotor $u_i \in \mathrm{S}^2$, $r_i \in \Re^3$, and $\gamma\sigma_i u_i \in \Re^3$.

2) pointing to any direction, while maintaining its posture against side-way wind (e.g., 360° camera shooting and fire-fighting hose operation); and
3) flying while adjusting its attitude at the same time (e.g., navigation in a pipe-cluttered environment).

The key challenge for this system is the very tight thrust margin and weight budget under the currently available motor and battery technologies, while being required to be fully functioning with all the components on-board and no power cable tethered to the ground. For this, on top of using lightweight/stiff carbon-fiber structures and weight-reducing 3-D-printed parts, we propose a general design optimization framework for the ODAR system, which optimizes the pose of the rotors to maximize the minimum-guaranteed omnidirectional force and torque generation with such an important aspect as interrotor aerodynamic interference and task-specific anisotropy incorporated. We also propose a novel selective mapping algorithm to substantially subdue the destabilizing effect of "ESC-induced singularity," i.e., temporary loss of thrust when the reversible rotor changes its rotating direction due to the lack of position sensing (i.e., sensorless BLDC), which, if not treated properly, can render the ODAR system behavior fairly shaky, unstable, and even resulting in a crash. With all these implemented, we also perform experiments, in which our eight-rotor ODAR system can exert downward force larger than 60 N much larger than its own weight (around 2.6 kg), can control its tip position and force at the same time (i.e., hybrid position/force control) while fixing its attitude, and can even attain a peg-in-hole task of its circular bar-end of 20 mm diameter into a 21 mm diameter hole via bilateral teleoperation. All these levels of aerial manipulation performance, we believe, are reported in this paper for the first time.

There have been proposed several new designs of flying platforms to overcome the issue of under-actuation [5]–[14]. The works of [5]–[8] advocate the use of extra actuators to tilt the direction of some or all of the rotors to overcome the issue of underactuation. However, adding those extra actuators, possibly as many as the rotors, can substantially increase the system complexity and also result in further reduction of the already fairly tight payload of the systems. The work of [9] presents a new aerial platform, the so-called spherically connected multiquadrotor (SmQ) system, which is actuated by multiple drones connected by passive spherical joints to the platform, thereby, can deal with both the underactuation and payload problems. This SmQ system, yet, still cannot exert a downward force larger than its own weight due to the unilateral thrust generation of the standard drones. More closely related to our proposed ODAR system are the designs of [10]–[14], where rotors attached with nonparallel directions are used to attain the full-actuation on SE(3) with no extra actuation. The works of [10]–[12] however optimize (or adjust) only the direction of the six rotors in S^1 while leaving their positions to be the same as those of the standard hexarotors. Although their designs achieve the full-actuation on SE(3), since their search space (i.e., S^1 of each rotor) is much narrower than ours (i.e., $\Re^3 \times \mathrm{S}^2$ of each rotor), given the tight weight budget and thrust margin of currently available motor and battery technologies, they would generate much less force/thrust omnidirectionally than our ODAR system, which may be adequate for just standalone flying in a mild environment (e.g., microgravity [12]), yet, likely substantially lacking for the manipulation tasks as demonstrated in this paper. The work of [13] optimizes both the S^2-orientation and the position of the rotors as done here, yet, their goal is not to maximize the wrench generation but to minimize the system size under the full-actuation constraint. Thus, similar as for [10]–[12], its wrench generation would be likely deficient for the manipulation tasks of this paper. In fact, the implementation of this design [13] (and also [11], [12]) has not been reported yet. Most closely related to our ODAR system is the design of [14], which also maximizes the omnidirectional wrench generation. However, it does not take into account the interrotor aerodynamic interference, which not only significantly affects the rotor performance but also results in infeasibility of their design, i.e., positions of some rotors are overlapped, thus heuristically relocated to some vertices of a cube in [14]. In contrast, we optimize both the position and the orientation of each rotor, while fully incorporating such important aspects as the interrotor aerointerference and gravity compensation. Furthermore, to our knowledge, the level of performance of the aerial manipulation tasks demonstrated in this paper (e.g., maximum downward force larger than 60 N; aerial peg-in-hole with radial tolerance of 0.5 mm) is unprecedented. We also believe that the issue of ESC-induced singularity is addressed in this paper for the first time with the selective mapping algorithm to substantially alleviate its destabilizing effect.

Some portions of this paper were presented in [15], which yet was only for the tethered ODAR system with six rotors and the manipulation experiment was limited only for the downward pushing task. In this paper, we extend the result of [15] to the untethered eight-rotor ODAR system while fully elaborating how to resolve and utilize its actuation redundancy with the closed-form expression of infinity-norm optimal control allocation. The peculiar issue of ESC-induced singularity and its stabilizing selective mapping are also presented here for the first

time, along with the hybrid pose/wrench control experiment and the teleoperated peg-in-hole experiment, which have not been reported elsewhere either.

The rest of the paper is organized as follows. Mechanical design and design optimization of the ODAR system are presented in Section II, and its dynamics modeling and control methods are briefly explained in Section III. The infinity-norm optimal control allocation and the selective mapping algorithm to stabilize the ESC-induced singularity are delineated in Section IV. Hardware setup and experiment results are presented in Section V, and some concluding remarks are given in Section VI.

II. Mechanical Design

A. Design Description

We design the ODAR system to be of the bar shape (see Fig. 1); since, first, it can conveniently hold or attach on itself tools commonly used for many operation and manipulation tasks (e.g., screw-driver, drill, inspection probe, etc.) while effectively resisting the reaction moment of the tool through its longitudinal length and, second, it can also mitigate the ground effect stemming from the fluid–structure interaction when the task takes place in a proximity of structures (e.g., close to wall, under the bridge girder, etc.), as the half of the actuators are located far from the interacting plane, it can still produce ample correcting wrench to subdue such a ground effect (see Section V). Of course, depending on task objectives, other shapes (e.g., spherical or disc shapes) would be desirable, for which the framework proposed in this paper can also be applied.

To construct the ODAR system, with an inspiration from the design of conventional drones, we adopt each pair of two symmetrically attached rotors as the basic actuator unit. More precisely, see Fig. 1, where the rotors 1 and 5 constitute such an actuator unit, with their rotor directions $u_1 = u_5 \in \mathrm{S}^2$ to be the same and their attachment locations $r_1 = -r_5 \in \Re^3$ symmetric w.r.t. the mainframe origin, while they rotate in different direction (e.g., their rotor types $\sigma_1 = 1$ and $\sigma_5 = -1$). With this symmetry, each rotor pair can then generate a 1-D control force (e.g., $(\lambda_1 + \lambda_5)u_1$, where λ_i is the rotor thrust output) and 1-D control torque (e.g., $(\lambda_1 - \lambda_5)[r_1 \times u_1 + \gamma\sigma_1 u_1]$, where $\gamma > 0$ is the thrust–yaw ratio caused by the drag force), independently and separately. This then implies that we can render the ODAR system fully actuated on SE(3) by using the three rotor pairs. This adoption of the rotor pairs as actuator units turns out to significantly simplify the process of design optimization (see Section II-B).

For the ODAR system to be omnidirectional, we also adopt reversible ESCs with the reversible propellers composed of two unidirectional props (i.e., with four blades) stacked together in the opposite direction (see Fig. 1). We also experimentally checked (see Fig. 7) that our stacked props, even with the inter-props flow interference, can still retain about 92% of the thrust production capability of a single unidirectional prop (with two blades). This reversible thrust generation is crucial particularly for aerial manipulation, since, only with that, we can exert a downward pushing force larger than the weight of the system itself, an impossible feat with typical multirotor drones with unidirectional rotors.

One of the foremost challenges of the ODAR design is that, under the current available motor and battery technologies, the weight–thrust budget of the ODAR is fairly tight, particularly for untethered operation. This in fact spurs us to adopt the eight-rotor design of Fig. 1 for untethered operation in this paper instead of the six-rotor design for tethered operation in [15], since, with batteries, electronics, cables, etc., all on-board, we could not find some a commercially available rotor–battery combination to fly our ODAR system with enough omnidirectional wrench-exerting capability. This eight-rotor design provides the actuation redundancy, which can be utilized, e.g., to better allocate control actuation to each rotor or to ameliorate the issue of zero-crossing of the reversible ESC (see Section IV). With this tight weight–thrust budget constraint, it turns out to be of paramount importance to optimize the pose of the rotors as best as possible to maximize omnidirectional wrench generation, which is the topic of Section II-B.

B. Wrench-Maximizing Design Optimization

The goal of our design optimization here is to decide the attaching location $r_i \in \Re^3$ and the thrust generation direction $u_i \in \mathrm{S}^2$ of each rotor, $i = 1, .., n$, all expressed in the body frame $\{B\}$, to maximize omnidirectional wrench generation (see Fig. 1). Using each pair of symmetrically attached rotors as an actuator unit as stated in Section II-A, we first define the sets of u_i and r_i s.t.

$$\mathcal{U} := \left\{ u_i \in \mathrm{S}^2 \,|\, u_j = u_{j+\frac{n}{2}},\, i = 1, \ldots, n, j = 1, \ldots, \frac{n}{2} \right\}$$

$$\mathcal{R} := \left\{ r_i \in \mathcal{R}_{\max} \,|\, r_j = -r_{j+\frac{n}{2}},\, i = 1, \ldots, n, j = 1, \ldots, \frac{n}{2} \right\}$$

where n is the total number of rotors, which is assumed to be even, and $\mathcal{R}_{\max}$ is the maximum allowable volume for all the rotor locations defined by

$$\mathcal{R}_{\max} := \left\{ r \in \Re^3 \,|\, \sqrt{r_y^2 + r_z^2} \le R_{\max},\, |r_x| \le \frac{L_{\max}}{2} \right\}$$

where $r = [r_x; r_y; r_z]$ expressed in $\{B\}$, and $R_{\max}$ and $L_{\max}$ are the maximum radius and length of the bar shape ODAR system, respectively. The type of rotors (i.e., left-handed or right-handed) is also considered as the optimization variable, since it affects the control torque generation via drag-induced reaction moment. For this, we define the set of rotor types as the optimization variable s.t.

$$\mathcal{S} := \left\{ \sigma_i \in \{1, -1\} \,|\, \sigma_j = -\sigma_{j+\frac{n}{2}},\, i = 1, \ldots, n, j = 1, \ldots, \frac{n}{2} \right\}$$

where $\sigma_i = 1$ means that the rotor generates upward thrust when rotating in clockwise direction (i.e., left-handed), and $\sigma_i = -1$ when in counterclockwise direction (i.e., right-handed). The search space of our design optimization is then given by $\mathcal{U} \times \mathcal{R} \times \mathcal{S}$.

Let us denote the torque generation of the jth rotor with the unit thrust generation (i.e., $\lambda_j = 1$) by

$$t_j := r_j \times u_j + \gamma\sigma_j u_j \in \Re^3 \tag{1}$$

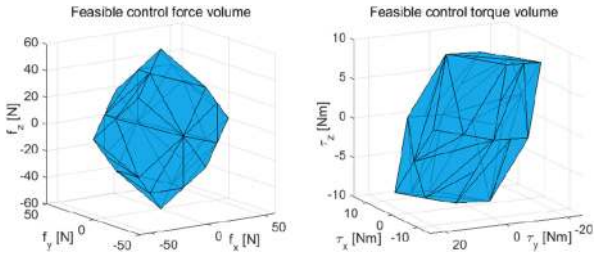

Fig. 2. Feasible control force and torque volume $(\mathcal{V}_\mathcal{F}, \mathcal{V}_\mathcal{M})$ of the optimally designed eight-rotor ODAR system in Fig. 1.

where $\gamma \approx 0.02$ for our case, according to experiments. We can then see that, under the definitions of $(\mathcal{U}, \mathcal{R}, \mathcal{S})$ mentioned above, $t_j = -t_{j+n/2}$, implying that each pair of the rotors j and $j + \frac{n}{2}$ can produce the 1-D control force $(\lambda_j + \lambda_{j+\frac{n}{2}}) \cdot u_j$ and the 1-D control torque $(\lambda_j - \lambda_{j+\frac{n}{2}}) \cdot t_j$ independently by adjusting their thrust outputs λ_j and $\lambda_{j+\frac{n}{2}}$, as stated in Section II-A. With this design symmetry, the search space for the optimization becomes square root of the nonsymmetric one, thereby substantially reducing the complexity of solving the design optimization.

Our design optimization then boils down to the problem of finding (u_j, r_j, σ_j) of each rotor pair to maximize the feasible control force volume $\mathcal{V}_\mathcal{F}$ and feasible control torque volume $\mathcal{V}_\mathcal{M}$ defined as follows:

$$\mathcal{V}_\mathcal{F} := \left\{ f \in \Re^3 \,|\, f = \sum_{i=1}^{n} \lambda_i u_i \,,\, \lambda_{\min} \le \lambda_i \le \lambda_{\max} \right\}$$

$$\mathcal{V}_\mathcal{M} := \left\{ \tau \in \Re^3 \,|\, \tau = \sum_{i=1}^{n} \lambda_i t_i \,,\, \lambda_{\min} \le \lambda_i \le \lambda_{\max} \right\}$$

where λ_i is the thrust output of the ith rotor; $\lambda_{\min}, \lambda_{\max} \in \Re$ are the minimum and maximum thrusts, respectively, for each rotor with $\lambda_{\max} = -\lambda_{\min} \ge 0$. Here, we assume uniformity among all the rotors. The sets $\mathcal{V}_\mathcal{F}$ and $\mathcal{V}_\mathcal{M}$ are both convex, since $\lambda_i u_i$ and $\lambda_i t_i$ each constitutes a convex set (see Fig. 2).

The ODAR system is purposed to be omnidirectional. Thus, it is desired to maximize the minimum force and torque generation by the system for any attitude. Of particular importance is to generate force for any attitude larger than its own weight so that the system can fly in any attitude. For this, we define the guaranteed minimum control force for any orientation (generated collectively by all the rotors) s.t., with $\mathcal{N}_h := \{1, 2, ..., n/2\}$,

$$\mathcal{F}_{\min}(\mathcal{U}) := \min_{i,j \in \mathcal{N}_h} \sum_{k \in \mathcal{N}_h} 2\lambda_{\max} \frac{|(u_i \times u_j)^T u_k|}{||u_i \times u_j||} \qquad (2)$$

which is the maximum radius of spheres centered at the origin and fully contained within the volume $\mathcal{V}_\mathcal{F}$. More specifically, consider the plane on $\mathcal{V}_\mathcal{F}$ spanned by u_i, u_j. Then, similar to the procedure developed for cable-driven robots in [16], the distance from the origin to this plane along its normal vector $u_i \times u_j$ can be written as, with $i, j \in \mathcal{N}_h$,

$$d^\mathcal{F}_{F_{ij}} = \sum_{k \in S_{ij}} 2\lambda_{\max} \frac{(u_i \times u_j)^T u_k}{||u_i \times u_j||} + \sum_{k \in \tilde{S}_{ij}} 2\lambda_{\min} \frac{(u_i \times u_j)^T u_k}{||u_i \times u_j||}$$

where $S_{ij}, \tilde{S}_{ij}$ are defined by

$$S_{ij} := \{k | (u_i \times u_j)^T u_k \ge 0\,,\, k \in \mathcal{N}_h\},\ \tilde{S}_{ij} := \mathcal{N}_h \setminus S_{ij}$$

and the multiplication by 2 of the right-hand side in the expression of $d^\mathcal{F}_{F_{ij}}$ is from our adoption of the rotor pairs. Then, since $\mathcal{V}_\mathcal{F}$ is convex with the origin in its interior as stated above, and further, symmetric w.r.t. the origin due to $\lambda_{\max} = -\lambda_{\min}$, we have $\mathcal{F}_{\min}(\mathcal{U}) = \min_{i,j \in \mathcal{N}_h} d^\mathcal{F}_{F_{ij}}$, from which (2) follows.

Nominally, the ODAR system is aimed to be omnidirectional. However, depending on task objectives or its shape, it may be more advantageous to endow it with the ability of anisotropic force/torque generation ability so that its performance along the more often-used attitude is enhanced, while that for the less-trotted attitude relaxed. For instance, the bar shape of our ODAR system naturally leads to the idea of using it more often with its pitch-yaw rotations (i.e., orientation about E-axis or D-axis in Fig. 1) instead of with its roll-rotation. In this case, it would be more desirable to "shape" the force generation capability in such a way that the force generation is maximized in the (N, D)-plane (i.e., sagittal plane) while relaxing along the E-axis expressed in $\{B\}$. Note that, even so, such roll-directional operations as screwdriving or drilling can still (and more conveniently) be achieved by simply attaching a rotating-tool with reaction moment succumbed to by the ODAR control torque generation.

This "anisotropic shaping" of the force generation can be attained by using the following weighted $\mathcal{F}^W_{\min}(\mathcal{U})$ in the place of $\mathcal{F}_{\min}(\mathcal{U})$ in (2):

$$\mathcal{F}^W_{\min}(\mathcal{U}) := \min_{i,j \in \mathcal{N}_h} \sum_{k \in \mathcal{N}_h} 2\lambda_{\max} \frac{|(W^{-1}u_i \times W^{-1}u_j)^T W^{-1} u_k|}{||W^{-1}u_i \times W^{-1}u_j||}$$

where $W := \mathrm{diag}[W_x, W_y, W_z]$ is the weight matrix with $0 < W_\star \le 1$ (with (x, y, z) corresponding to (N, E, D) of $\{B\}$). Here, note that, if $W_\star < 1$, $\mathcal{V}_\mathcal{F}$ will be stretched by $1/W_\star$ along that direction, $\mathcal{F}^W_{\min}(\mathcal{U})$ will be strengthened along that direction as compared to $\mathcal{F}_{\min}(\mathcal{U})$, thereby relaxing the force generation requirement along that direction. For instance, for our bar shape ODAR, we choose $W = [1, 0.4, 1]$ (see Table 1) so that the force generation requirement along the body-fixed E-axis is relaxed while retaining that for the (N, D)-plane. Although the ODAR system can still operate with $W = [1, 1, 1]$, we however found that this $W = [1, 0.4, 1]$ provides us a better-tuned ODAR system for the operations with more pitch/yaw-rotations as experimented in Section V.

On the other hand, for the control torque generation optimization, similar to (2), we can define the guaranteed minimum control torque for all the orientation (generated collectively by all the rotors) s.t.

$$\mathcal{M}_{\min}(\mathcal{U}, \mathcal{R}, \mathcal{S}) := \min_{i,j \in \mathcal{N}_h} \sum_{k \in \mathcal{N}_h} 2\lambda_{\max} \frac{|(t_i \times t_j)^T t_k|}{||t_i \times t_j||} \qquad (3)$$

or its weighted version $\mathcal{M}^V_{\min}(\mathcal{U}, \mathcal{R}, \mathcal{S})$ similar to $\mathcal{F}^W_{\min}$ stated above with the weight matrix $V := \mathrm{diag}[V_x, V_y, V_z]$ to attain the anisotropic torque generation capability. For our design below, we choose $V = [1, 1, 1]$.

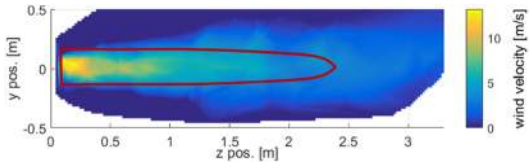

Fig. 3. Anemometer measurement of wind velocity distribution downstream the rotor generating thrust required for hovering with the rest pose ($R_{OB} = I$) with the r_a-function also marked with interference-threshold wind speed to be 4 m/s.

We can then formulate the design optimization problem as a constrained optimization problem for (u_i, r_i, σ_i) s.t.

$$\max_{\mathcal{R},\mathcal{S}} \quad \mathcal{M}^V_{\min}(\arg\max_{\mathcal{U}} \mathcal{F}^W_{\min}(\mathcal{U}), \mathcal{R}, \mathcal{S}) \tag{4}$$

$$\text{s.t.} \quad u_i^T u_i = 1,\ r_i \in \mathcal{R}_{\max} \tag{5}$$

$$\mathcal{F}^W_{\min}(\mathcal{U}) \geq mg,\ d_{\text{aero}}(\mathcal{U}, \mathcal{R}) \geq D \tag{6}$$

where (5) are to constrain $u_i \in \mathrm{S}^2$ and to constrain the volume of the ODAR system; (6) are to ensure that the ODAR system can fly while overcoming its own weight (with the relaxation endowed by $W = [W_x, W_y, W_z]$ as discussed above) and reducing the interrotor aerodynamic interference by ensuring that the gap between the flow stream of each rotor (i.e., $\mathcal{C}_{a,i}$) and other rotors (i.e., r_j) be larger than a certain value D, i.e., $d_{\text{aero}}(\mathcal{U}, \mathcal{R}) := \min_{i,j} ||c_{a,i} - r_j|| \geq D$, $c_{a,i} \in \mathcal{C}_{a,i}$, where $i, j \in \{1, 2, ..., n\}$, $i \neq j$ and $\mathcal{C}_{a,i}(r_i, R_{BU_i}) := \{c \in \Re^3 | c = R_{BU_i} v + r_i,\ \sqrt{v_x^2 + v_y^2} \leq r_a(v_z)\}$ is the flow stream volume of the ith rotor, with $R_{BU_i} \in \mathrm{SO}(3)$ being the rotation matrix from $\{B\}$ to $\{U_i\}$ (see Fig. 1), $v := [v_x; v_y; v_z] \in \Re^3$ a position vector in $\{U_i\}$, and $r_a : \Re \to \Re$ being the axial shape function of the aerodynamic space also similarly used in [13]. To identify this flow-axial function r_a, we perform an experiment to measure wind velocity distribution downstream the rotor generating thrust required for hovering with the rest pose ($R_{OB} = I$). See Fig. 3, from which we obtain the r_a-function to be a tapered cylinder as marked therein. For this, we choose the interference-threshold wind velocity to be 4 m/s (i.e., gentle breeze according to the Beaufort scale, known to be adequate for drone flying).

We solve this constrained optimization (4)–(6), and the obtained optimal ODAR design is illustrated in Fig. 1 with its feasible control force and torque volumes $\mathcal{V}_\mathcal{F}$ and $\mathcal{V}_\mathcal{M}$ also shown in Fig. 2. Since the optimization problem (4)–(6) is nonconvex and has a complex form of objective and constraints, the solution is obtained with the grid search method. Note also from (4) that we first determine the thrust directions $u_i \in \mathrm{S}^2$ of all the rotors, and then solve for their attaching location $r_i \in \Re^3$ and their types σ_i given the obtained $u_i \in \mathrm{S}^2$. This *sequential formulation* turns out to significantly speed up the solving process of the optimization (4)–(6) while still providing an adequate design as experimentally validated in Section V.

Design parameters and optimized design variables are summarized in Table I, where only those of the rotors 1–4 are given due to the symmetric design of the ODAR system. For this optimization, we also assume $\lambda_{\max} = 9.7\,\text{N}$ according to the specification of the rotors used in the implementation (see Section V-A). With this rotor thrust, the ODAR system can overcome its weight along the (N, D)-plane, as the minimum guaranteed control force within this sagittal (N, D)-plane is $F^{xz}_{\min}(\mathcal{U}) = 37.35\,\text{N}$, whereas the weight of the ODAR system is 25.48 N (i.e., 2.6 kg—see Section V-A). Here, note that the omnidirectionally guaranteed minimum force $F_{\min}(\mathcal{U}) = 17.97\,\text{N}$ is less than the weight of the system, even if we enforce (6). This is because we use the weight $W = [1, 0.4, 1]$ to relax the force generation along the body-fixed E-axis as our ODAR system will be used mostly with minimal roll-rotation as stated above and also experimentally validated in Section V. With $W = [1, 1, 1]$, we can ensure $F_{\min}(\mathcal{U}) > 25.48\,\text{N}$, yet with deterioration of the force generating capability in the sagittal plane. See Fig. 2 also for the feasible control force and torque volumes $\mathcal{V}_\mathcal{F}$ and $\mathcal{V}_\mathcal{M}$ with the metric information endowed by $\lambda_{\max}$ with the omnidirectionally guaranteed minimum control torque to be 8.67 N·m.

TABLE I
DESIGN OPTIMIZATION PARAMETERS AND OPTIMIZED VALUES

Symbols	Values	Units
n	8	-
$R_{\max}$	0.24	m
$L_{\max}$	0.8	m
W	$\text{diag}[1, 0.4, 1]$	-
V	$\text{diag}[1, 1, 1]$	-
D	0.12	m
$\mathcal{F}_{\min}(\mathcal{U})$	$2.04\lambda_{\max}$	N
$\mathcal{F}^{xz}_{\min}(\mathcal{U})$	$3.85\lambda_{\max}$	N
$\mathcal{M}_{\min}(\mathcal{U}, \mathcal{R}, \mathcal{S})$	$0.894\lambda_{\max}$	Nm
$d_{\text{aero}}(\mathcal{U}, \mathcal{R})$	0.125	m
$\mathcal{U}$	$u_1 = [0.68; 0.28; 0.68]$ $u_2 = [0.68; 0.28; -0.68]$ $u_3 = [0.68; -0.28; 0.68]$ $u_4 = [0.68; -0.28; -0.68]$	-
$\mathcal{R}$	$r_1 = [0.40; -0.17; 0.17]$ $r_2 = [0.40; 0.17; 0.17]$ $r_3 = [0.40; -0.17; -0.17]$ $r_4 = [0.40; 0.17; -0.17]$	m
$\mathcal{T}$	$t_1 = [-0.15; -0.15; 0.24]$ $t_2 = [-0.18; 0.38; 0.01]$ $t_3 = [-0.18; -0.38; -0.01]$ $t_4 = [-0.18; 0.16; -0.21]$	m
$\mathcal{S}$	$\sigma_1 = +1,\ \sigma_2 = -1,$ $\sigma_3 = -1,\ \sigma_4 = -1$	-

III. SYSTEM MODELING AND CONTROL DESIGN

With the design optimization of Section II-B, which determines u_i, r_i, and σ_i to maximize the guaranteed minimum force $\mathcal{F}^W_{\min}$ and torque $\mathcal{M}^V_{\min}$ for any attitude, we can model the ODAR system as a fully actuated rigid body s.t.

$$\begin{aligned} m\ddot{x} &= R_{OB} B_f \lambda - mge_3 + f_e \\ J\dot{\omega} + \omega \times J\omega &= B_\tau \lambda + \tau_e \end{aligned} \tag{7}$$

where $m > 0$ is the mass with $x \in \Re^3$ being the center-of-mass position expressed in $\{O\}$, $J \in \Re^{3\times3}$ is the inertia matrix with $\omega \in \Re^3$ being the angular velocity expressed in $\{B\}$, and g is the gravitational constant with $e_3 = [0; 0; 1]$(see Fig. 1). Also, $\lambda = [\lambda_1; \lambda_2; \cdots; \lambda_n] \in \Re^n$ is the collection of the thrust inputs of all rotors, and $B_f, B_\tau \in \Re^{3\times n}$ are the mapping matrices from the thrust inputs to the control force and control torque, with their

ith column respectively specified by $B_f^i := u_i$, $B_\tau^i := t_i$ where $u_i, t_i \in \Re^3$ are the 1-D space of the thrust and torque generation of the ith rotor (see Section II-B).

For notational convenience, we define

$$\begin{pmatrix} f \\ \tau \end{pmatrix} := \begin{bmatrix} R_{OB} & 0 \\ 0 & I_{3\times3} \end{bmatrix} \begin{bmatrix} B_f \\ B_\tau \end{bmatrix} \lambda =: \bar{R}B\lambda \tag{8}$$

where $f, \tau \in \Re^3$ are the translation and orientation controls respectively expressed in $\{O\}$ and $\{B\}$, $\bar{R} := \text{diag}[R_{OB}, I_{3\times3}] \in \Re^{6\times6}$, and $B := [B_f; B_\tau] \in \Re^{6\times n}$ is the mapping matrix, which is to be full row rank, as the design optimization in Section II-B enforces the full-actuation of the ODAR system on SE(3). This then means that we can design the control wrench $(f, \tau) \in \Re^6$ for various control objectives as if the system is fully actuated on SE(3), and then allocate this $(f, \tau) \in \Re^6$ to $\lambda \in \Re^n$ while exploiting the redundancy for some other purposes (e.g., to avoid thrust saturation and thrust loss when rotors cross zero speed (see Section IV).

In this paper, the following three control objectives are implemented: pose trajectory tracking on SE(3), hybrid pose/wrench control, and bilateral teleoperation for peg-in-hole task. Since the control design of fullyactuated rigid systems on SE(3) is a well-studied subject, we only provide here a brief explanation for each of these. For the pose trajectory tracking on SE(3), we adopt the standard proportional-integral-derivative control in E(3) and also that for SO(3) as proposed in [17] to avoid singularity in SO(3) during the omnidirectional motion of the ODAR system. This pose tracking control can also serve as the basis of impedance control, as the ODAR system is back-drivable. For the hybrid pose/wrench control, we use the standard approach as presented in [18] along with the momentum-based observer [19] to estimate the external wrench exerted on the system.

For the teleoperation, we utilize the passive set-position modulation (PSPM [20], [21]) at the ODAR-side along with the pose tracking PD-control, which turns out to significantly improve the overall teleoperation stability by smoothly modulating abrupt changes of the human command. At the master-side, a simple combination of tracking error and external wrench similar to that in [21] for UAVs is provided to the user as the haptic feedback. Here, even with the PSPM only inserted at the ODAR-side, the teleoperation stability can be ensured, since the communication delay is negligible and the force feedback gain not so aggressive. This teleoperation, particularly with its haptic feedback and 3-D visual information, turns out crucial to attain precision peg-in-hole task by exploiting human learning of the full dynamics of the ODAR system, which is too complicated to be modeled (e.g., aerodynamics, fluid–structure interaction, etc) and, thus, cannot be controlled with such aprecision in a fully autonomous manner(see Section V).

IV. Control Allocation With Selective Mapping

A. Infinity-Norm Minimization

Once the desired control wrench $w := [f; \tau] \in \Re^6$ is calculated as stated in Section III, it needs to be distributed among the n-rotor commands $\lambda = (\lambda_1, \lambda_2, ..., \lambda_n) \in \Re^n$ to produce $U = B\lambda$, where $U := [R_{OB}^T f; \tau] = \bar{R}^{-1}w \in \Re^6$ from (8). Here, we assume $n \geq 8$ as stated in Section II-A; thus, the actuation redundancy should be addressed as well. The most commonly used method for this is to minimize the two norm of $\lambda \in \Re^n$ i.e., $\lambda_o = B^\dagger U$, where $B^\dagger := B^T(BB^T)^{-1} \in \Re^{n\times6}$. Although also adopted in [14] and relevant to power efficiency to some extent, this two-norm optimization is not so suitable for the ODAR system, since, with the rotor actuation margin fairly tight, only one rotor saturation can simply result in instability and even crash, which is not captured by the two-norm optimization. To address this issue, here, we adopt the infinity-norm optimization for (8), which can be written by

$$\begin{aligned} \lambda_\alpha &:= B^\dagger U + N_B \xi' \\ \xi' &:= \underset{\xi \in \Re^{n-6}}{\arg\min} ||B^\dagger U + N_B \xi||_\infty \end{aligned} \tag{9}$$

where $\lambda_\alpha \in \Re^n$ is the thrust vector to be used, $N_B \in \Re^{n\times(n-6)}$ is the kernel of the mapping matrix B, and $\xi' \in \Re^{n-6}$ is the null vector component. This infinity-norm optimization has been extensively studied for many applications (e.g., for robot manipulators [22]), yet is known in general not to assume a closed-form solution.

For the eight-rotor ODAR system optimally designed as shown in Fig. 1, it turns out that we can attain the closed-form of the infinity-norm optimization (9) with a slight modification of the design. More precisely, we change σ_1 in Table I from $\sigma_1 = 1$ to $\sigma_1 = -1$. With this $\sigma_1 = -1$, we then have the same optimal design of Table I for (4)–(6) , except $\mathcal{T} = \{t_1 = [-0.18; -0.16; 0.21], t_2 = [-0.18; 0.38; 0.01], t_3 = [-0.18; -0.38; -0.01], t_4 = [-0.18; 0.16; -0.21]\}$. With this modified design, the minimum guaranteed control force remains the same (since $\mathcal{U}$ is not changed), whereas the minimum guaranteed control torque is reduced only by 3.6%. Further, the design then satisfies the following condition with $\nu = [1; -1; -1; 1]$, which is used for the computation of a closed-form solution as summarized in Proposition 1

$$\begin{aligned} B_{f,\star}\nu := 0,\ B_{\tau,\star}\nu = 0,\ B_{f,r} = B_{f,l},\ B_{\tau,r} = -B_{\tau,l} \\ \nu := [\nu_1; \nu_2; \nu_3; \nu_4]\,,\ |\nu_i| = 1\,,\ i \in \mathcal{N}_h \end{aligned} \tag{10}$$

where $\star \in \{r, l\}$ (with r-side with rotors 1–4 and l-side with rotors 5–8; see Fig. 1) and $B =: [B_{f,r}\ B_{f,l}; B_{\tau,r}\ B_{\tau,l}]$, $B_{f,\star}, B_{\tau,\star} \in \Re^{3\times4}$.

Proposition 1: Consider the mapping matrix $B \in \Re^{6\times8}$ of (8) for the ODAR system with $n = 8$. If this B-matrix satisfies the properties (10), the solution of the infinity-norm optimization (9) is given by

$$\begin{aligned} \lambda_\alpha &= B^\dagger U + N_B \begin{bmatrix} \xi'_r \\ \xi'_l \end{bmatrix} \\ \xi'_\star &= -\tfrac{1}{2}(\lambda^\nu_{\star,\max} + \lambda^\nu_{\star,\min}) \end{aligned} \tag{11}$$

where $\star \in \{r, l\}$, $\lambda^\nu_\star := \text{diag}(\nu)\lambda_{o,\star} \in \Re^4$ with $\lambda_o := B^\dagger U = [\lambda_{o,r}; \lambda_{o,l}] \in \Re^8$; and $\lambda^\nu_{\star,\max}, \lambda^\nu_{\star,\min}$ are the maximum and minimum component of $\lambda^\nu_\star$.

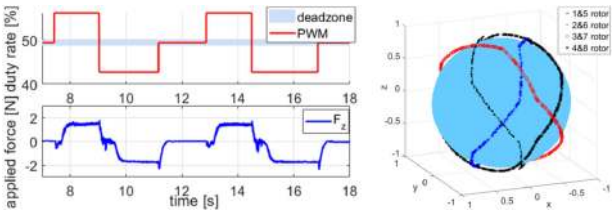

Fig. 4. (Left) Plot of input PWM to the ESC and resultant force generated by the bidirectional rotor when the desired direction of force is suddenly changed (around 9 and 14.5 s). (Right) Slicing of S^2-sphere by the zero-thrust lines of the rotor pairs of the eight-rotor ODAR system. Note that two pairs of the rotors simultaneously become zero-thrust only at certain points on S^2.

Proof: Under the properties of (10), the kernel matrix of the B-matrix can be written as

$$N_B = \begin{bmatrix} \nu & 0 \\ 0 & \nu \end{bmatrix} \in \Re^{8\times 2} \tag{12}$$

where $\nu = [1; -1; -1; 1] \in \Re^4$. We can then attain, from (11), that

$$|\lambda_{\alpha,\star,i}| = |\lambda_{o,\star,i} + \nu_i \xi'_\star| = |\nu_i \lambda_{o,\star,i} + \xi'_\star| \tag{13}$$

where $\star \in \{r, l\}$, $i \in \mathcal{N}_h$, $\xi'_\star \in \Re$, and $\lambda_\alpha =: [\lambda_{\alpha,r}; \lambda_{\alpha,l}]$. Then, the infinity-norm of $\lambda_{\alpha,\star}$ is given by

$$\begin{aligned} ||\lambda_{\alpha,\star}||_\infty &= \max(|\max(\lambda_{\alpha,\star})|, |\min(\lambda_{\alpha,\star})|) \\ &= \max(|\lambda^\nu_{\star,\max} + \xi'_\star|, |\lambda^\nu_{\star,\min} + \xi'_\star|) \end{aligned}$$

which is minimized when $\xi'_\star$ is selected s.t.

$$\lambda^\nu_{\star,\max} + \xi'_\star = -(\lambda^\nu_{\star,\min} + \xi'_\star)$$

Finally, note that $||\lambda_\alpha||_\infty = \max(||\lambda_{\alpha,r}||_\infty, ||\lambda_{\alpha,l}||_\infty)$, which is also minimized with the above selection of $\xi'_\star$, since the kernel matrix N_B has the block-diagonal structure and ξ'_r, ξ'_l only affects $||\lambda_{\alpha,r}||_\infty, ||\lambda_{\alpha,l}||_\infty$, respectively. ■

We will use this solution of (11) as a basis of the control allocation for further adjustment of λ_i to mitigate the issue arising from the zero-crossing of the rotor as stated in Section IV-B.

B. ESC-Induced Singularity and Selective Mapping

Once we applied the allocated thrust input λ_α of (11) to the ODAR system for the hovering, at certain attitudes, the system behavior becomes fairly shaky and, in some cases, even goes unstable and results in a crash. This we found stems from the phenomenon that the BLDC motors of the rotors slow-down and re-rotate when they are commanded to suddenly change their rotation direction (see Fig. 4), where the rotors "hesitate" when changing their rotating directions (around 9.5 and 14.5 s). This hesitation is due to the lack of position sensing of the BLDC rotor motors, i.e., typical off-the-shelf drone rotor ESCs are not equipped with position sensors (e.g., hall sensor) and instead rely on the back electromotive force to estimate the rotor position for their control, which becomes not so useful when the rotor speed gets close to zero. Typical ESCs in fact utilize their own certain "bootstrapping" algorithm to start rotation due to this lack of position sensing. Even though position sensors can be embedded into the rotor BLDC motors, in this paper, we consider the case of the sensorless BLDC rotors, since, to our knowledge, all the commercially available drone ESCs are all sensorless, likely due to the added complexity and cost of extra hall sensors.

Shown in Fig. 4 is the slicing of S^2 (pitch and yaw) by the zero-thrust lines of some rotor pairs when the eight-rotor ODAR of Fig. 1 stays hovering quasi-statically while changing its attitude, where the two rotors of each pair experience the zero thrust at the same time due to the symmetry of the ODAR design and the hovering operation. Fig. 4 then shows that the zero-crossing of some rotors is likely inevitable for any omnidirectional operation of the ODAR system, since the system needs to sweep through arbitrarily on this S^2-sphere. When the system passes through these zero-thrust lines, some of its rotors would not be properly functioning, possibly resulting in deterioration of the performance, loss of full-actuation on SE(3) and even unstable behavior as stated above. Due to this reason, given a task, we call the zero-thrust points on SO(3) of the ODAR system as "ESC-induced singularity."

Now, for this ESC-induced singularity, we propose a novel *selective mapping* algorithm, which, by exploiting the actuation redundancy of the ODAR system, can "propel" at least six rotors far from this singularity and map the desired control wrench $U \in \Re^6$ of (11) to these six rotors to maintain the full-actuation on SE(3) while deactivating the control mapping to the (at most) two rotors that are allowed to be close to the zero-thrust point by the algorithm with some interpolation to enhance the smoothness of this process. Here, we choose to propel only the six rotors away from the singularity rather than all the eight rotors, since pushing all the eight rotors away from the zero-thrust point necessitates more thrust generation of all the rotors, which turns out too large to be accommodated by our ODAR system with its rotor thrust-generation margin already so tight and six rotors can still provide the full-actuation on SE(3).

More precisely, for the modified eight-rotor ODAR system as stated in Section IV-A, we first modulate λ_α of (11) such that the thrust magnitude of at least three rotor pairs is larger than a certain thrust margin $\epsilon_1 > 0$ from the zero-thrust line

$$\lambda_\beta := B^\dagger U + N_B\left(\xi' + \xi''(\lambda_\alpha)\right) \tag{14}$$

$$\xi''_\star(\lambda_\alpha) = \arg\min_{\xi_\star \in \Re} |\xi_\star - \xi''_{\star,\text{pre}}|$$

$$\text{s.t.} \sum_{i=1}^{4} \text{sgn}\left(|\lambda_{o,\star,i} + \nu_i(\xi'_\star + \xi''_\star)| - \epsilon_1\right) \geq 3 \tag{15}$$

where $\star \in \{r, l\}$, $\xi''(\lambda_\alpha) := [\xi''_r; \xi''_l] \in \Re^2$, $\xi''_{\star,\text{pre}} \in \Re$ is the solution from the previous step, and expression (15) comes from the structure of (13) with $\nu = [1; -1; -1; 1]$. Here, note that the modulation of ξ'' is done along the column space of the null matrix N_B, which has the form of (12) with $\nu = [1; -1; -1; 1]$ for the modified ODAR system of Section IV-A. This then implies that the optimization of (14) is always feasible, since, by increasing $|\xi''_\star|$, we can always "propel" $\lambda_{\alpha,\star}$ along the lines specified by $\nu_r = [1; -1]$ and $\nu_l = [-1; 1]$ outside the set $|\lambda_{\alpha,\star,i}| < \epsilon_1$

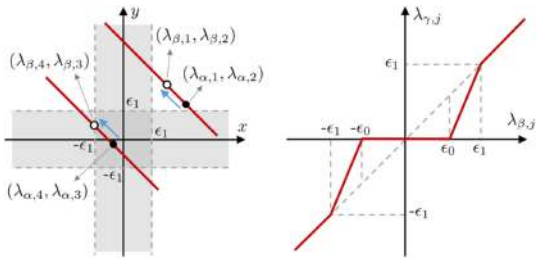

Fig. 5. (Left) Geometric structure of the λ_β-modulation (14): the r-side $\lambda_{\beta,r} = (\lambda_{\beta,1}, \lambda_{\beta,2}, \lambda_{\beta,3}, \lambda_{\beta,4})$ is propelled from the black dots along $\nu_r = [1; -1]$ and $\nu_l = [-1; 1]$ so that only $|\lambda_{\beta,3}| < \epsilon_1$ with the other three larger than ϵ_1. (Right) Thrust thresholds $0 < \epsilon_0 < \epsilon_1$ to gradually switch from the full-use if $|\lambda_{\beta,j}| > \epsilon_1$ to the complete-disuse if $|\lambda_{\beta,j}| < \epsilon_0$ with a linear interpolation between them.

(see Fig. 5). This optimization (14) can be quickly solved, since the objective function and the constraint are all based on linear functions.

Once the λ_β-modulation of (14) is performed, for each r-side and l-side of the ODAR system, we have at most one rotor with its thrust magnitude less than ϵ_1, while the other (at least) three rotors guaranteed to be away from the zero-thrust point farther than ϵ_1. To avoid the ESC-induced singularity, it is then better to stop using those rotors with near-zero thrust, yet, it is not desirable either to suddenly stop using them in view of control smoothness. For this, we define ϵ_0 with $0 < \epsilon_0 < \epsilon_1$ to gradually switch from the full-utilization of the jth rotor if $|\lambda_{\beta,j}| \geq \epsilon_1$ to its complete-disuse if $|\lambda_{\beta,j}| < \epsilon_0$, with a smooth interpolation between them (see Fig. 5).

For the modified eight-rotor ODAR system as stated in Section IV-A, this gradually switching selective mapping can be written as follows. For this, suppose first that the jth and kth rotor in the r-side and the l-side of the ODAR system in Fig. 1, respectively, are designated as the "near-zero" rotors via (14), i.e., $|\lambda_{\beta,j}| < \epsilon_1$ and $|\lambda_{\beta,k}| < \epsilon_1$ with the thrust magnitude of all the other six rotors larger or equal to ϵ_1. Here, we allow $j = \emptyset$ or $k = \emptyset$. Then, we further modulate λ_β of (14) s.t.

$$\lambda_\gamma := \bar{B}^\dagger(\lambda_\beta)U + \bar{N}_B(\lambda_\beta)(\xi' + \xi''(\lambda_\alpha)) \tag{16}$$

with

$$\bar{B}^\dagger(\lambda_\beta) := \begin{bmatrix} e_r B_r^\dagger + (1-e_r)B_{r\backslash\{j,k\}}^\dagger \\ e_l B_l^\dagger + (1-e_l)B_{l\backslash\{j,k\}}^\dagger \end{bmatrix} \in \Re^{8\times 6}$$

$$\bar{N}_B(\lambda_\beta) := \begin{bmatrix} e_r\nu & 0 \\ 0 & e_l\nu \end{bmatrix} \in \Re^{8\times 2}$$

and

$$e_\star := \begin{cases} 1 & \text{if } |\min_{i\in\mathcal{N}_h}(|\lambda_{\beta,\star,i}|)| > \epsilon_1 \\ \dfrac{\min_{i\in\mathcal{N}_h}(|\lambda_{\beta,\star,i}|) - \epsilon_0}{\epsilon_1 - \epsilon_0} & \text{if } \epsilon_1 \geq |\min_{i\in\mathcal{N}_h}(|\lambda_{\beta,\star,i}|)| > \epsilon_0 \\ 0 & \text{if } \epsilon_0 \geq |\min_{i\in\mathcal{N}_h}(|\lambda_{\beta,\star,i}|)| \end{cases}$$

for $\star \in \{r, l\}$, where $B_r^\dagger, B_l^\dagger \in \Re^{4\times 6}$ are defined by $[B_r^\dagger; B_l^\dagger] := B^\dagger \in \Re^{8\times 6}$, and $B_{r\backslash\{j,k\}}^\dagger, B_{l\backslash\{j,k\}}^\dagger \in \Re^{4\times 6}$ by $B_{\backslash\{j,k\}}^\dagger =: \left[B_{r\backslash\{j,k\}}^\dagger; B_{l\backslash\{j,k\}}^\dagger\right] \in \Re^{8\times 6}$, where $B_{\backslash\{j,k\}}^\dagger := I_{\backslash\{j,k\}}B^T(BI_{\backslash\{j,k\}}B^T)^{-1}$ is the reduced mapping matrix excluding the jth and kth rotors with $I_{\backslash\{j,k\}} \in \Re^{8\times 8}$ being the identity matrix with the jth and kth diagonal elements set to be zero. Here, $(BI_{\backslash\{j,k\}}B^T)^{-1}$ is nonsingular from the structure of $B_r, B_l \in \Re^{3\times 4}$ and $BB_{\backslash\{j,k\}}^\dagger = I$.

When the properties of (10) are granted, as true for the modified eight-rotor ODAR system explained in Section IV-A, we then have the following "decoupling" property:

$$B_{r\backslash\{j,k\}}^\dagger = B_{r\backslash j}^\dagger,\ B_{l\backslash\{j,k\}}^\dagger = B_{l\backslash k}^\dagger \tag{17}$$

where $B_{r\backslash j}^\dagger, B_{l\backslash k}^\dagger \in \Re^{4\times 6}$ are defined by

$$B_{\backslash j}^\dagger =: \left[B_{r\backslash j}^\dagger; B_l^\dagger\right],\ B_{\backslash k}^\dagger =: \left[B_r^\dagger; B_{l\backslash k}^\dagger\right] \tag{18}$$

where $B_{\backslash i}^\dagger := I_{\backslash i}B^T(BI_{\backslash i}B^T)^{-1}$. Here, if $j = \emptyset$ or $k = \emptyset$, $B_{r\backslash j}^\dagger = B_r^\dagger$ (with $e_r = 1$) or $B_{l\backslash k}^\dagger = B_l^\dagger$ (with $e_l = 1$). This then means that the selective mapping matrix $B_{\star\backslash\{j,k\}}^\dagger$ for (16) can be computed for the r-side (i.e., $B_{r\backslash j}^\dagger$) and the l-side (i.e., $B_{l\backslash k}^\dagger$) as if they are decoupled from each other. This decoupling property (17)–(18) also turns out crucial to render the gradually switching selective mapping (16) to be exact (i.e., produce the desired control wrench U regardless of e_r, e_l), as summarized in Proposition 2.

Proposition 2: Consider the mapping matrix $B \in \Re^{6\times 8}$ of (8) for the eight-rotor ODAR system. Then, if the properties of (10) are satisfied, the following statements hold.

1) The decoupling property (17)–(18) is grant.
2) The mapping (16) is exact, i.e., $B\lambda_\gamma = U, \forall e_r, e_l$.

Proof: Write $B^\dagger = [B_{r,f}^\dagger\ B_{r,\tau}^\dagger; B_{l,f}^\dagger\ B_{l,\tau}^\dagger]$, where $B_{\star,*}^\dagger \in \Re^{4\times 3}$, $\star \in \{r, l\}$ and $* \in \{f, \tau\}$. By using the Sherman–Morrison formula, $B_{\backslash\{j,k\}}^\dagger$ in (17)–(18) can be expanded s.t.

$$\begin{aligned} B_{\backslash\{j,k\}}^\dagger &= I_{\backslash\{j,k\}}B^T(BI_{\backslash\{j,k\}}B^T)^{-1} \\ &= I_{\backslash\{j,k\}}\left(B^\dagger - B^\dagger BI_{\{j,k\}}S^{-1}I_{\{j,k\}}B^\dagger\right) \end{aligned} \tag{19}$$

where $I_{\{j,k\}} := I_{8\times 8} - I_{\backslash\{j,k\}} \in \Re^{8\times 8}$ and $S := I_{8\times 8} + I_{\{j,k\}}B^\dagger BI_{\{j,k\}}$.

Here, we first show that $B^\dagger B$ is block diagonal. For this, we write

$$B^\dagger B = \frac{1}{2}\begin{bmatrix} B_{\star,f}^\dagger B_{f,\star} + B_{\star,\tau}^\dagger B_{\tau,\star} & B_{\star,f}^\dagger B_{f,\star} - B_{\star,\tau}^\dagger B_{\tau,\star} \\ B_{\star,f}^\dagger B_{f,\star} - B_{\star,\tau}^\dagger B_{\tau,\star} & B_{\star,f}^\dagger B_{f,\star} + B_{\star,\tau}^\dagger B_{\tau,\star} \end{bmatrix}$$

due to the property of (10), where $\star \in \{r, l\}$. Further, since they share the same null-vector $\nu \in \Re^4$ in (10), we can write

$$B_{f,\star} = B_{f,\star\backslash a}L,\ B_{\tau,\star} = B_{\tau,\star\backslash a}L$$

where $a \in \mathcal{N}_h$ is an index s.t. $\nu_a \neq 0$; $B_{f,\star\backslash a}, B_{\tau,\star\backslash a} \in \Re^{3\times 3}$ are matrices obtained by discarding the ath column from $B_{f,\star}, B_{\tau,\star}$, and $L \in \Re^{3\times 4}$ is the constant matrix specified by ν of (10). Here, since $B_{f,\star}, B_{\tau,\star}$ are designed to be full row-rank (i.e., 3) for the full-actuation on SE(3), $B_{f,\star\backslash a}$ and $B_{\tau,\star\backslash a}$ are also full rank and invertible. We can then obtain $B_{\star,f}^\dagger B_{f,\star} = B_{\star,\tau}^\dagger B_{\tau,\star} ==$

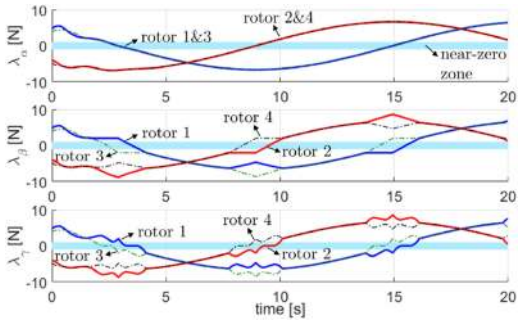

Fig. 6. Selective mapping process: $\lambda_{\alpha,i}$ (thrust value after infinity-norm minimization), $\lambda_{\beta,i}$ (thrust value after full-actuation preserving modulation), and $\lambda_{\gamma,i}$ (thrust value after excluding zero-crossing rotors) during the pitching rotation motion. Only $\lambda_{\star,i}$ of the r-side rotors are shown for brevity.

$L^T(LL^T)^{-1}L$, and further

$$B^\dagger B = \mathrm{diag}[L^T(LL^T)^{-1}L, L^T(LL^T)^{-1}L].$$

Then, since $B^\dagger B$ is block diagonal and also only the jth and kth rows of $I_{\{j,k\}}S^{-1}I_{\{j,k\}}B^\dagger$ are nonzero, the upper four rows of $B^\dagger_{\setminus\{j,k\}}$ in (19) are the same as those of $B^\dagger_{\setminus j}$, whereas its lower four rows are the same as those with $B^\dagger_{\setminus k}$. If we set $k=\emptyset$ or $j=\emptyset$, $B^\dagger_{\setminus\{j,k\}} = B^\dagger_{\setminus j}$ or $B^\dagger_{\setminus\{j,k\}} = B^\dagger_{\setminus k}$, which still retain the same structure of $B^\dagger_{\setminus\{j,k\}}$. This completes the proof of the first item.

For the second item, recall that $BB^\dagger = B_rB_r^\dagger + B_lB_l^\dagger = I$. Also, from the decoupling property (17)–(18), we have

$$BB^\dagger_{\setminus j} = B_rB^\dagger_{r\setminus j} + B_lB_l^\dagger = I$$

where $B^\dagger_{\setminus j} = I_{\setminus j}B^T(BI_{\setminus j}B^T)^{-1}$ with $(BI_{\setminus j}B^T)^{-1}$ being invertible from the structure of B_r, B_l as stated above for $B^\dagger_{\setminus\{j,k\}}$. This, and the similar derivation for $BB^\dagger_{\setminus k}$, implies that

$$B_rB_r^\dagger = B_rB^\dagger_{r\setminus j},\ B_lB_l^\dagger = B_lB^\dagger_{l\setminus k}$$

with which we have

$$B\bar{B}^\dagger = e_rB_rB_r^\dagger + (1-e_r)B_rB^\dagger_{r\setminus j} + e_lB_lB_l^\dagger + (1-e_l)B_lB^\dagger_{l\setminus k}$$
$$= I + e_r(B_rB_r^\dagger - B_rB^\dagger_{r\setminus j}) + e_l(B_lB_l^\dagger - B_lB^\dagger_{l\setminus k}) = I$$

completing the proof of the second item. ■

The infinity-norm optimization (11) and the selective mapping process (14) and (16) are shown in Fig. 6, where $\lambda_{\alpha,i}$, $\lambda_{\beta,i}$, and $\lambda_{\gamma,i}$ are plotted during a pitching rotation simulation of the modified eight-rotor ODAR system, which in fact passes through the intersection of the two zero-thrust lines in Fig. 4. Only those for the r-side rotors are shown here with that of the l-side omitted for brevity. From Fig. 6, we can then see that, first, $(\lambda_{\beta,1}, \lambda_{\beta,3})$ split around 3 and 14 s, whereas $(\lambda_{\beta,2}, \lambda_{\beta,4})$ around 8 s, preventing simultaneous zero-crossing of multiple rotors and allowing only for one rotor thrust magnitude to be less than ϵ_1, while that of the other three larger than ϵ_1, thereby ensuring the full-actuation on SE(3); and, second, through the process of (16), the $\lambda_{\gamma,i}$ behaves around near-zero boundary more smoothly than $\lambda_{\beta,i}$, while the rotors with near-zero thrust are gradually switched to disuse and, when $|\lambda_{\beta,i}| < \epsilon_o$, their thrust is set to zero according to (16) (e.g., $\lambda_{\gamma,1} = 0$ around 3 and 16 s). See also Fig. 11 for the experimental result of this selective mapping.

Fig. 7. Thrust generation of the rotor with one single unidirectional prop (dashed line) and with two unidirectional props stacked in the opposite direction (solid line).

It is worthwhile to mention that, even if it is exact as proved in Proposition 2, this selective mapping, in general, can only alleviate the effect of the ESC-induced singularity and does not completely eliminate it, although it can stabilize the ESC-induced singularity through all of our experiments and simulations. This is because the selective mapping formulates "dynamic" ESC-induced singularity as "static" entities, i.e., it decides its action only based on the rotor thrust input $\lambda_{\alpha,i}(t)$, although the real rotor thrust $\lambda_i(t)$ is the output of the ESC bootstrapping control-logic (with its own dynamics) given $\lambda_{\alpha,i}(t) \approx 0$ (see Fig. 4). Due to this reason, the ODAR system should be designed in such a way that the target operations mostly take place as far from the ESC-induced singularity as possible, and that crossing zero-thrust lines is permitted with the selective mapping, yet only in a reserved manner. How to incorporate the ESC-induced singularity with its full dynamics and nonlinearity is a topic of active research by itself (i.e., control optimization with dynamic constraint) and is a topic of our future research as well.

V. Experiments

A. System Setup

As stated in Sections II-B and IV-A, we implement the modified eight-rotor ODAR as shown in Fig. 1, whose main bar-frame is constructed by using a commercial carbon fiber pipe of 20 mm diameter and 1.5 mm thickness, making the length of the total system to be 1.2 m. Eight BLDC motors (MN3508-KV700 from T-Motor) are attached to the mainframe via 3-D-printed parts, according to the design optimization of Section II-B. To achieve bidirectional rotors, we stack two unidirectional props (each with two blades, diameter 10 in and pitch 4.7 in) in the opposite direction and drive them together by a reversible ESC (DYS-XMS30A with BLHeli firmware). We also perform an experiment to check the thrust generation of this bidirectional rotor and achieve the result as shown in Fig. 7, which shows that this bidirectional rotor can produce thrust about 92% of that of the single prop, which is up to 9.7 N for both the upward and downward directions. To provide enough current to all the eight rotors, we adopt a four-cell Li-Po battery (14.8 V, 4000 mAh, 45 C) along with a switching battery eliminator circuit (SBEC) to power up other modules (e.g., computing, communication, etc.) with 5 V. For the computing, a microcontroller unit (MCU) board equipped with Cortex-M4 CPU (STM32F429IG from

STMicroelectronics) is used. The central vacancy of the mainframe contains these battery, MCU, and other modules to make the geometric center coincident to the mass center as close as possible. With all these, the final ODAR system is achieved as shown in Fig. 1 with a weight of 2.6 kg. See also Section II-B for the other system specifications.

The MCU board then receives the pose data from a motion capture system (VICON Bonita-B3) via WiFi (2.4 GHz) with 125 Hz, which is fused with the gyroscope measurement of an IMU sensor (MPU-9250) with 200 Hz via I^2C to obtain the attitude of the ODAR system through the SO(3) nonlinear complementary filter [23]. The desired pose for the control is computed in the MCU board, or, in the case of teleoperation, received from a 6-DOF haptic device (Phantom Premium 6DOF) via WiFi with 125 Hz. External wrench is estimated with a wrench estimator [19] and also measured with a six-axis F/T sensor (RFT40-SA01, Robotous) as ground truth for the hybrid pose/wrench control. For teleoperation, we use the F/T sensor to avoid the implementation issue of communication (i.e., sending estimated wrench from MCU to the master device significantly slows down WiFi from MOCAP to MCU as well). With all the information as stated above, the MCU board calculates the desired control wrench (f, τ), as stated in Section III, and allocates it to the eight rotors via the infinity-norm optimization (see Section IV-A) modulated by the selective mapping (see Section IV-B) with 1 kHz, which is then converted to pulsewidth modulation (PWM) signal and sent to each reversible ESC.

B. Experimental Results

Using the ODAR system constructed as in Section V-A, we conduct the validating experiments of the three control laws of Section III: pose trajectory tracking; hybrid pose/wrench control; and PSPM-based peg-in-hole teleoperation. We also perform an experiment to show the efficacy of the selective mapping of Section IV-B for the pitching rotation with four rotors experiencing the ESC-induced singularity. Due to the page limit, here, we only present the (partial) results of the experiments mentioned above, compressively showing the indispensable results to explain the contributed works. We then refer readers to the accompanied video for full experimental results[1] including results of pose trajectory tracking, hybrid control, and peg-in-hole teleoperation with other attitude to thoroughly demonstrate the performance of the system.

The results of the hybrid pose/wrench control are shown in Fig. 8, where the modified eight-rotor ODAR system tracks the circular trajectory of 60 cm diameter with the angle-sweeping rate of 9°/s, while maintaining the vertical attitude and pushing down the horizontal board with 10 N. The RMS errors of the position, angle, and force tracking are obtained to be 3.04 cm, 1.01°, and 0.82 N. For this, we can clearly see that the ODAR system is fully actuated on SE(3). We also find that the system can fairly stably interact with the board even with substantial ground-flow effect, which we believe is due to its bar-shape. We

[1]Also, available at `https://youtu.be/S3i9NspWtr0`

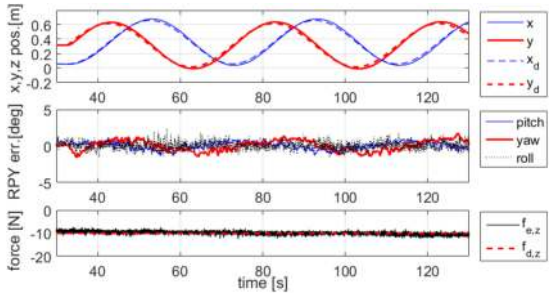

Fig. 8. Hybrid pose/wrench control: pose tracking error and contact force regulation performance ($f_{e,z}$ and $f_{d,z}$ denote measured and desired applied forces in the z-direction) while drawing the circle on the horizontal plane.

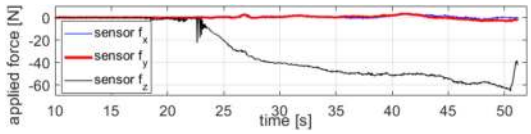

Fig. 9. Contact force measurement during the "pushing-down" experiment, where the ODAR system can exert a 64 N downward force, substantially larger than its own weight (2.6 kg).

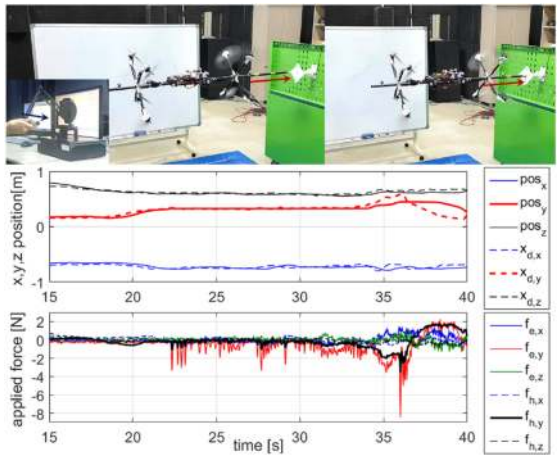

Fig. 10. Peg-in-hole teleoperation. (Top) System position x and human command x_d. (Bottom) Measured external force f_e and haptic force feedback f_h.

also perform the "pushing-down" experiment, where the ODAR system position is held while increasing its downward force. The measurement of this contact force is shown in Fig. 9, where we can see that the ODAR system can exert up to 64 N, which significantly exceeds its own weight (2.6 kg), an impossible feat for standard drone-manipulator systems only with unidirectional thrust generation.

The results of the PSPM-based peg-in-hole teleoperation are shown in Fig. 10, where the ODAR system is teleoperated by a human user in such a way that the end of its carbon-fiber tube with the diameter of 20 mm is inserted into a 3-D-printed hole of a diameter of 21 mm. This level of task precision (i.e., radial tolerance of 0.5 mm) is by far beyond the achievable by some fully autonomous control as demonstrated in the above-mentioned hybrid control experiment (i.e., RMS positioning

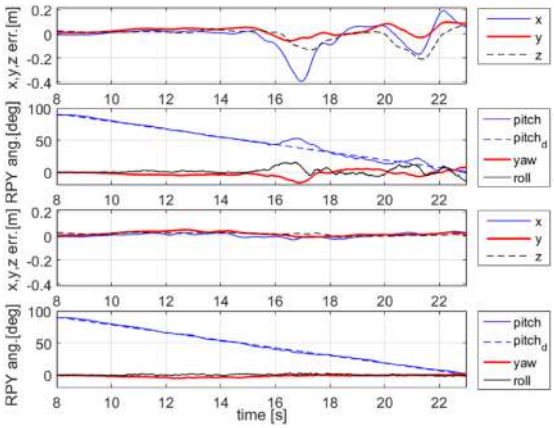

Fig. 11. Pitching-rotation with the center-of-mass position and other attitudes hold: without selective mapping (top two plots) and with selective mapping (bottom two plots).

error of 3.04 cm). This we believe is because the system dynamics with rotor aerodynamics, fluid–structure interaction, motor dynamics, unmodeled structural dynamics, etc. is too complicated to be modeled in a mathematically tractable way. Even so, with the teleoperation, the human user can succeed this precision peg-in-hole task from the first contact (around 22 s) to its full insertion (around 36 s). This we believe is because human users somehow can "learn" those complicated physics and incorporate that into their commanding strategy to properly react to those complicated physics of the system, thereby, successfully guiding its dynamics into the peg-in-hole completion. For this, we also find the 3-D visual information and the force feedback are imperative, without which the human users find it very difficult to achieve this task.

The last experiment is to show the efficacy of the selective mapping in Section IV-B to subdue the instability stemming from the ESC-induced singularity. For this, the ODAR system is controlled to rotate from 90° pitch angle (i.e., vertical posture) to 0° pitch angle (i.e., horizontal posture), while maintaining its center-of-mass position and other attitude angles stationary, and inducing the zero-thrust crossing of four rotors at the same time, as shown in Fig. 4. The experiment results in Fig. 11 show that without the selective mapping, the behavior of the ODAR systems becomes so shaky (e.g., wobbling around 17 and 21 s), resulting in the failure of the pitching rotation experiment (eventually unstable crash if not stopped by hands); and with the selective mapping, this shaky and unstable behavior is successfully subdued and the ODAR system can finish the vertical-to-horizontal pitching rotation.

VI. Conclusion

We propose a new aerial manipulation platform, ODAR, which can produce omnidirectional motion and wrench (i.e., full-actuation in SE(3)). To address the tight thrust margin and weight budget of current motor and battery technologies, we present a design optimization framework, which incorporates such important aspects as interrotor aerointerference, anisotropic task requirement, etc. Closed-form infinity-norm optimal control allocation and selective mapping algorithm are also proposed to address the tight thrust saturation margin and the ESC-induced singularity of sensorless BLDC rotors. With all these, the ODAR system exhibits the following unprecedented level of performance and capability: separate position and orientation control on SE(3); hybrid pose/wrench control with downward force of 60 N much larger than its own weight (2.6 kg); and peg-in-hole force feedback teleoperation with radial tolerance of 0.5 mm. Some possible future research topics include the following: sensor fusion using a camera or a global navigation satellite system for MOCAP-less flying; a control algorithm to fully address "dynamic" ESC-induced singularity; and miniaturization and swarming of multiple ODAR systems.

References

[1] A. E. Jimenez-Cano *et al.*,"Control of an aerial robot with multi-link arm for assembly tasks," in *Proc. IEEE Int. Conf Robot. Autom.*, 2013, pp. 4916–4921.

[2] C. Korpela, M. Orsag, M. Pekala, and P. Oh, "Dynamic stability of a mobile manipulating unmanned aerial vehicle," in *Proc. IEEE Int. Conf. Robot. Autom.*, 2013, pp. 4922–4927.

[3] H. Yang and D. J. Lee, "Dynamics and control of quadrotor with robotic manipulator," in *Proc. IEEE Int. Conf. Robot. Autom.*, 2014, pp. 5544–5549.

[4] H. Yang and D. Lee, "Hierarchical cooperative control framework of multiple quadrotor-manipulator systems," in *Proc. IEEE Int. Conf. Robot. Autom.*, 2015, pp. 4656–4662.

[5] M. Ryll, H. H. Bülthoff, and P. R. Giordano, "Modeling and control of a quadrotor UAV with tilting propellers," in *Proc. IEEE Int. Conf. Robot. Autom.*, 2012, pp. 4606–4613.

[6] Y. Long and D. J. Cappelleri, "Linear control design, allocation, and implementation for the omnicopter MAV," in *Proc. IEEE Int. Conf. Robot. Autom.*, 2013, pp. 289–294.

[7] A. Oosedo *et al.*, "Flight control systems of a quad tilt rotor unmanned aerial vehicle for a large attitude change," in *Proc. IEEE Int. Conf. Robot. Autom.*, 2015, pp. 2326–2331.

[8] M. Ryll, D. Bicego, and A. Franchi, "Modeling and control of FAST-Hex: A fully-actuated by synchronized-tilting hexarotor," in *Proc. IEEE/RSJ Int. Conf. Intell. Robot Syst.*, 2016, pp. 1689–1694.

[9] H.-N. Nguyen, S. Park, J. Park, and D. J. Lee, "A novel robotic platform for aerial manipulation using quadrotors as rotating thrust generators," *IEEE Trans. Robot.*, vol. 34, no. 2, pp. 353–369, Apr. 2018.

[10] G. Jiang and R. Voyles, "A nonparallel hexrotor UAV with faster response to disturbances for precision position keeping," in *IEEE Int. Symp. Safety, Security Rescue Robot.*, Hokkaido, Japan, 2014, pp. 1–5.

[11] S. Rajappa, M. Ryll, H. H. Bülthoff, and A. Franchi, "Modeling, control and design optimization for a fully-actuated hexarotor aerial vehicle with tilted propellers," in *Proc. IEEE Int. Conf. Robot. Automat.*, 2015, pp. 4006–4013.

[12] P. Roque and R. Ventura, "Space cobot: Modular design of an holonomic aerial robot for indoor microgravity environments," in *Proc. IEEE/RSJ Int. Conf. Intell. Robot. Syst.*, 2016, pp. 4383–4390.

[13] A. Nikou, G. C. Gavridis, and K. J. Kyriakopoulos, "Mechanical design, modelling and control of a novel aerial manipulator," in *Proc. IEEE Int. Conf. Robot. Automat.*, 2015, pp. 4698–4703.

[14] D. Brescianini and R. D'Andrea, "Design, modeling and control of an omni-directional aerial vehicle," in *Proc. IEEE Int. Conf. Robot. Automat.*, 2016, pp. 3261–3266.

[15] S. Park, J. Her, J. Kim, and D. J. Lee, "Design, modeling and control of omni-directional aerial robot," in *Proc. IEEE/RSJ Int. Conf. Intell. Robot. Syst.*, 2016, pp. 1570–1575.

[16] P. Bosscher, A. T. Riechel, and I. Ebert-Uphoff, "Wrench-feasible workspace generation for cable-driven robots," *IEEE Trans. Robot.*, vol. 22, no. 5, pp. 890–902, Oct. 2006.

[17] F. Goodarzi, D. Lee, and T. Lee, "Geometric nonlinear PID control of a quadrotor UAV on SE(3)," in *Proc. IEEE Eur. Control Conf.*, 2013, pp. 3845–3850.

[18] R. M. Murray, Z. Li, and S. S. Sastry, *A Mathematical Introduction to Robotic Manipulation*. Boca Raton, FL, USA: CRC, 1993.

[19] T. Tomić, C. Ott, and S. Haddadin, "External wrench estimation, collision detection, and reflex reaction for flying robots," *IEEE Trans. Robot.*, vol. 33, no. 6, pp. 1467–1482, Dec. 2017.
[20] D. J. Lee and K. Huang, "Passive-set-position-modulation framework for interactive robotic systems," *IEEE Trans. Robot.*, vol. 26, no. 2, pp. 354–369, Apr. 2010.
[21] D. J. Lee *et al.*, "Semiautonomous haptic teleoperation control architecture of multiple unmanned aerial vehicles," *IEEE/ASME Trans. Mechatron.*, vol. 18, no. 4, pp. 1334–1345, Aug. 2013.
[22] Y. Zhang, "Inverse-free computation for infinity-norm torque minimization of robot manipulators," *Mechatronics*, vol. 16, no. 3, pp. 177–184, 2006.
[23] R. Mahony, T. Hamel, and J.-M. Pflimlin, "Non-linear complementary filters on the special orthogonal group," *IEEE Trans. Autom. Control*, vol. 53, no. 5, pp. 1203–1218, Jun. 2008.

Sangyul Park received the B.S. degree in mechanical and aerospace engineering from Seoul National University, Seoul, South Korea, in 2013, where he is currently working toward the Ph.D. degree in mechanical engineering.

His research interests include design, modeling, and control of aerial robotic systems.

Jeongseob Lee received the B.S. degree in mechanical and aerospace engineering from Seoul National University, Seoul, South Korea, in 2016, where he is currently working toward the Ph.D. degree in mechanical engineering.

His research interests include robot manipulator control and teleoperation.

Joonmo Ahn received the B.S. degree in mechanical and aerospace engineering from Seoul National University, Seoul, South Korea, in 2017, where he is currently working toward the M.S. degree in mechanical engineering.

His research interests include robot manipulator control and teleoperation.

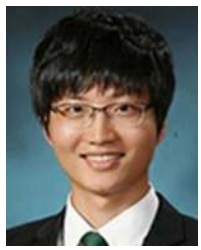

Myungsin Kim received the B.S. degree in mechanical and aerospace engineering from Seoul National University, Seoul, South Korea, in 2012, where he is currently working toward the Ph.D. degree in mechanical engineering.

His research interests include passivity-based haptic rendering and multiuser haptics.

Jongbeom Her received the B.S. degree in electronics and information engineering from Kyung Hee University, Suwon, South Korea, in 2010, and the M.S. degree in mechanical engineering from the Seoul National University, Seoul, South Korea, in 2016.

He is currently with Samsung Electronics, Suwon, South Korea. His research interests include robotics and autonomous flight systems.

Gi-Hun Yang received the B.S. and M.S. degrees in mechanical engineering from KAIST, Daejeon, South Korea, in 2000, 2002, and the Ph.D. degree in mechanical engineering from KAIST in 2008.

He was previously a Postdoctoral Researcher with the Center for Cognitive Robotics Research, KIST. He is currently a Principal Research Scientist with the Robotics Group at Korea Institute of Industrial Technology, Ansan, South Korea. His research interests include haptics, teleoperation, HRI, bioinspired robots, and industrial robotics.

Dongjun Lee received the B.S. degree in mechanical engineering from KAIST, Daejeon, South Korea, in 1995, the M.S. degree in automation and design from KAIST, Seoul, South Korea, in 1997, and the Ph.D. degree in mechanical engineering from the University of Minnesota at Twin Cities, Minnesota, USA, in 2004.

He is currently an Associate Professor with the Department of Mechanical and Aerospace Engineering, Seoul National University, Seoul, South Korea. His main research interests include dynamics and control of robotic and mechatronic systems with emphasis on teleoperation/haptics, aerial robots, multirobot systems and industrial control applications.